Nanoscale

ROYAL SOCIETY OF CHEMISTRY

COMMUNICATION

View Article Online
View Journal | View Issue

Cite this: *Nanoscale*, 2022, **14**, 8906

Received 7th April 2022,
Accepted 31st May 2022

DOI: 10.1039/d2nr01921c

rsc.li/nanoscale

Cupric porphyrin frameworks on multi-junction silicon photocathodes to expedite the kinetics of CO_2 turnover†

Zhihe Wei,[a,b] Qiaoqiao Mu,[a] Ronglei Fan,[b] Yanhui Su,[a] Yongtao Lu,[a] Zhao Deng,[a] Mingrong Shen *[b] and Yang Peng *[a]

Photoelectrochemical CO_2 reduction utilizing silicon-based photocathodes offers a promising route to directly store solar energy in chemical bonds, provoking the development of heterogeneous molecular catalysts with high turnover rates. Herein, an *in situ* surface transformation strategy is adopted to grow metal–organic frameworks (MOFs) on Si-based photocathodes, serving as catalytic scaffolds for boosting both the kinetics and selectivity of CO_2 reduction. Benefitting from the multi-junctional configuration for enhanced charge separation and the porous MOF scaffold enriching redox-active metalloporphyrin sites, the Si photocathode demonstrates a high CO faradaic efficiency of 87% at a photocurrent density of 10.2 mA cm^{-2}, which is among the best seen for heterogeneous molecular catalysts. This study highlights the exploitation of reticular chemistry and macrocycle complexes as Earth-abundant alternatives for catalyzing artificial photosynthesis.

Introduction

Mimicking the natural photosynthesis process, the utilization of intermittent solar power to convert anthropogenic CO_2 emissions into chemical fuels and feedstocks offers a one-stone-two-birds approach to simultaneously mitigate the greenhouse effect and resource crisis.[1,2] Among the various technical routes, photoelectrochemical CO_2 reduction (PEC CO_2R) is highly tempting owing to its obvious benefits in terms of the direct utilization of solar energy, avoidance of sacrificial agents, and less susceptibility to CO_2 mass transport, as well as the well-established photovoltaic technology tree.[3,4] Recent years have witnessed ascending efforts in fabricating PEC devices with diverse configurations to maximize the CO_2 turnover rate and product selectivity, which often involved noble metals and alloys such as Pt, Au, Ag/Cu, Au/Cu, *etc*. as electrocatalysts.[5–9] Nonetheless, the exploitation of noble metals is always plagued with high material and recycling costs, calling for the development of more economic and efficient catalysts based on Earth-abundant elements and compounds.

In catalyzing electrochemical CO_2 reduction reactions (CO_2RRs), heterogeneous molecular catalysts based on macrocycle complexes and reticular chemistry offer promising alternatives for the aforementioned noble metals in virtue of their tunable chemistry, well-exposed catalytic centers, and the capability to modulate the local electrolytic environment within the Helmholtz layer.[10,11] With explicit chemical structures, they also provide mechanistic understandings of the reaction mechanisms.[12,13] However, as of today there have been quite limited PEC studies on CO_2RRs adopting heterogeneous molecular catalysts, especially those based on non-precious metals.[14–16] In particular, metal–organic-frameworks (MOFs), assembled by metal ions/clusters as nodes and organic ligands as linkers, have attracted extensive attention over the past two decades.[17] Benefitting from their eminent advantages in porosity, absorptivity, and possession of isolated and under-saturated metal centers,[18] MOFs have shown great potential in gas sorption and separation,[19] electrocatalysis,[11] photocatalysis,[20] sensors,[21] biomedicine[22] and so on. However, they have been barely seen in the functionalization of photocathodes for the PEC CO_2RR, except for the one study conducted by Xiong *et al.*[23] Therein, HKUST-1 was coated on a Cu_2O photocathode for simultaneously preventing photocorrosion and promoting catalytic activities. Despite a low photocurrent density of less than 1 mA cm^{-2}, the authors carried out transient absorption measurements to attest to the promoted charge separation and transfer at the semiconductor/MOF interface. To the best of our knowledge, there have been no studies on applying MOFs to modify Si-based photocathodes for modulating the CO_2RR process.

[a]*Soochow Institute of Energy and Material Innovations, College of Energy, Soochow Municipal Laboratory for Lowe Carbon Technoliges and Industries, Soochow University, Suzhou 215006, China. E-mail: mrshen@suda.edu.cn*
[b]*School of Physical Science and Technology, Jiangsu Key Laboratory of Thin Films, Collaborative Innovation Center of Suzhou Nano Science and Technology, Soochow University, Suzhou 215006, China. E-mail: ypeng@suda.edu.cn*

† Electronic supplementary information (ESI) available. See DOI: https://doi.org/10.1039/d2nr01921c

In the current study, we demonstrate, for the first time, the adoption of MOFs as the catalytic scaffold on Si-based photocathodes for boosting both the kinetics and selectivity of PEC CO_2RRs. Several structural and engineering aspects have been concerned to optimize the light absorption and charge separation (Fig. 1a), including the adoption of an n^+–p Si photoabsorber with a buried p–n junction and surface texturing, the passivation by a TiO_2 interlayer to mitigate carrier recombination and promote charge extraction, as well as the deposition of a dispersive Cu overlayer to form a secondary Schottky junction to further relay the photoelectrons to the topmost MOF scaffold. Such a multi-junctional configuration of Si/TiO_2/Cu well complies with the direction of energy flow from the conduction band (CB) of Si (−4.05 eV *vs.* vacuum) to the CB of TiO_2 (−4.21 eV *vs.* vacuum), and further to the Fermi band of Cu (−4.61 eV *vs.* vacuum).[24–26] Moreover, the 3D porous framework and the isolated metalloporphyrin Cu centers of the MOF scaffold are capable of synergistically promoting both the CO_2RR kinetics and selectivity, resulting in an optimal CO faradaic efficiency of 87% at an extraordinary photocurrent density of 10.2 mA cm^{-2}, the latter being the highest ever observed for heterogeneous molecular catalysts for the PEC CO_2RR.

Results and discussion

The fabrication of MOF-functionalized n^+–p Si/TiO_2/Cu composite photocathodes and the topological structure of the Cu-TCPP(Cu) MOF are illustrated in Fig. 1a. The n^+–p Si with a buried p–n junction was textured with surface pyramidal arrays for promoting the light-harvesting efficiency, and was used as the photovoltaic base for its enhanced photovoltage and charge separation. On top of the p–n junction, a layer of TiO_2 was deposited through atomic layer deposition (Fig. S1†). This TiO_2 layer served as both the passivation layer for mitigating charge recombination at Si surface defects and the electron transfer layer for promoting electron extraction from the photoabsorber.[7,27,28] Additionally, it was utilized as the binder to enhance the binding strength of the thermally evaporated Cu film onto the Si substrate, adding a TiO_2/Cu Schottky junction. Such an n^+–p Si/TiO_2 configuration has been reported typically affording a photovoltage of ~550 mV.[7] A thin Cu film of ~50 nm (Fig. S2†), after being partially converted to Cu $(OH)_2$ nanowire arrays (Fig. S3†), served as the precursor for the *in situ* growth of Cu-TCPP (TCPP = tetrakis(4-carboxyphenyl)porphyrin) MOFs with and without metalloporphyrin Cu centers on the photocathodes, which are correspondingly denoted as SiTCM(Cu) and SiTCM. For comparison, the control samples of n^+–p Si/TiO_2/Cu and n^+–p Si/TiO_2 are respectively referred to as SiTC and SiT.

Fig. 1b and c display the top-view scanning electron microscopy (SEM) images of the as-prepared SiTCM(Cu) photocathode with different magnifications, exhibiting enormous thin sheets of the Cu-TCPP(Cu) MOF vertically orientated on pyramidal Si arrays. The cross-sectional image in Fig. 1d reveals a porous Cu layer underneath the thin MOF sheets, as

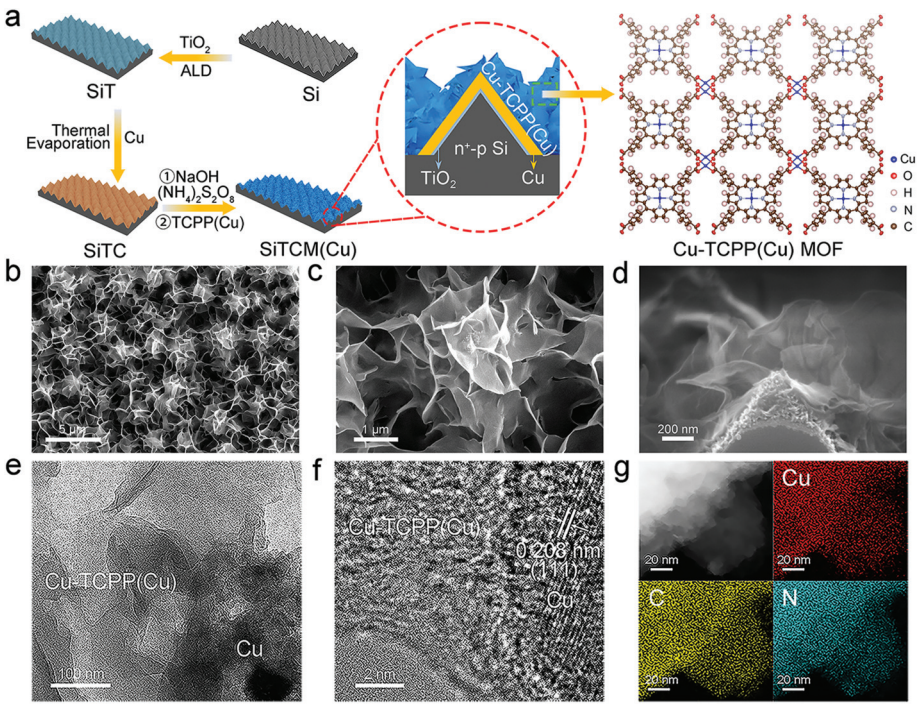

Fig. 1 Microstructural characterization of SiTCM(Cu). (a) Schematic diagrams illustrating the preparation of the SiT, SiTC and SiTCM(Cu) photocathodes and the topological structure of the Cu-TCPP(Cu) MOF. (b and c) Top-view SEM images of different magnifications and (d) the cross-sectional view taken on the SiTCM(Cu) photocathode. (e and f) TEM images of different magnifications obtained at the Cu/Cu-TCPP(Cu) interface. (g) EDX elemental mapping images of Cu, C and N on the MOF scaffold obtained by HAADF-STEM.

further evidenced by high-resolution transmission electron microscopy (TEM) images showing an intimate MOF/Cu interface (Fig. 1e and f). Specifically in Fig. 1f, the distinct lattice fringes with a *d*-spacing of 0.208 nm are ascribed to the Cu (111) plane,[29] whereas the amorphous structure on the left refers to the Cu-TCPP(Cu) MOF destructed by the TEM electron beam. Energy dispersive X-ray (EDX) mapping images (Fig. 1g) further revealed a uniform distribution of Cu, C and N on the surface scaffold, corroborating the formation of the Cu-TCPP (Cu) MOF. Likewise, SiTCM without metalloporphyrin Cu centers presented similar surface morphology to that of SiTCM (Cu) comprising vertically arrayed MOF thin sheets (Fig. S4†).

Fig. 2a shows a comparison of the attenuated total reflectance Fourier transform infrared (ATR-IR) spectra of SiTCM (Cu), SiTCM, SiTC and SiT, with the reference spectra of TCPP (Cu) and H_2TCPP ligands given in Fig. S5.† Note that a strong C═O stretching band at ~1707 cm^{-1} from –COOH was observed in the spectra of TCPP(Cu) and H_2TCPP, but absent from those of SiTCM(Cu) and SiTCM. Instead, two new bands at ~1610 and 1400 cm^{-1} emerged, owing to the formation of a $Cu_2(COO)_4$ "paddle-wheel" structure in the MOFs (see Fig. 1a for the schematics) as a result of node–ligand coordination.[30] The intensive Cu–N stretching bands at 1000 cm^{-1} provide strong evidence for the Cu-coordinated metalloporphyrins in both TCPP(Cu) and SiTCM(Cu), while the N–H fingerprints at ~980 cm^{-1} in the spectra of H_2TCPP and SiTCM are characteristic of freebase porphyrins.[31] In stark contrast, no absorption bands were observed from the ATR-IR spectrum of SiTC and SiT between 800 and 2000 cm^{-1} owing to their inorganic nature.

UV-vis diffuse reflectance spectra (DRS) (Fig. 2b) show that compared to SiT, SiTC exhibits a prominent absorption band at 550 nm resulting from the deposited Cu layer.[32] Besides, the overall UV-vis absorption on SiTC is weaker due to the enhanced light reflection on the Cu surface. SiTCM displays one strong Soret band and four Q bands that are characteristic of free-base porphyrins. In comparison, SiTCM(Cu) only shows two Q bands, which are typical of metalloporphyrins with improved coordination symmetry.[31] Compared to SiTCM, the Soret band of SiTCM(Cu) is blue-shifted toward a lower wavelength as a result of the shifted π^* orbital energy. Overall, the light absorbance on the MOF-modified photocathodes is notably enhanced, likely due to the eroded Cu coating and the intrinsic absorbance by porphyrins. Both the Raman spectra of SiT and SiTC display only one Si peak in the wavenumber range of 200–1700 cm^{-1} without any vibrational signatures from Cu and TiO_2 (Fig. 2c). In stark contrast, SiTCM and SiTCM(Cu) present a library of vibrational modes, mainly inherited from the spectra of H_2TCPP and TCPP(Cu), respectively (Fig. S6†). In general, the number of vibrational modes observed on both TCPP(Cu) and SiTCM(Cu) is less than that on H_2TCPP and SiTCM, which is again ascribed to the enhanced symmetry of metalloporphyrins.

X-ray photoelectron spectra (XPS) taken on SiTCM(Cu) unveiled two Cu oxidation states namely Cu^{2+} and Cu^0, respectively ascribed to the Cu-TCPP(Cu) MOF and the underlying Cu substrate (Fig. 2d).[33] The N 1s spectrum can be deconvoluted into two well-resolved peaks at 398.6 and 399.9 eV, attributed to metalloporphyrin Cu–N and the pyrrolic nitrogen (–N═) species, respectively (Fig. 2e).[34] Taken together, all the above morphological and spectroscopic evidence on SiTCM and SiTCM(Cu) unanimously testify to the successful transformation of the Cu surface into a Cu-MOF, forming a Si/TiO_2/Cu/MOF multi-junction, and the only difference between the two lies in the presence/absence of central Cu–N coordination in the porphyrin rings.

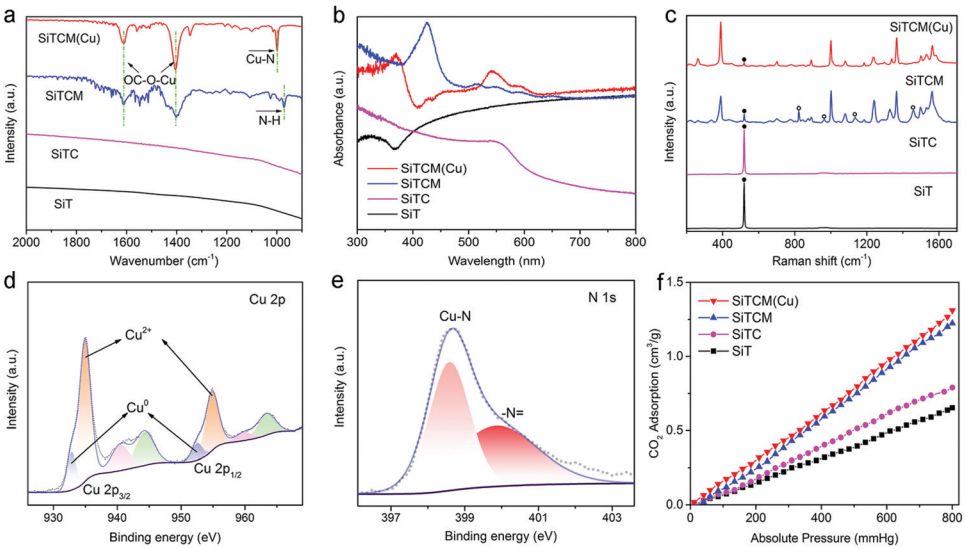

Fig. 2 Physicochemical characterization studies of SiT, SiTC, SiTCM and SiTCM(Cu). (a) ATR-IR, (b) UV-vis diffuse reflectance and (c) Raman spectra (● marks the Si peak and ○ marks the peaks unique to SiTCM). High-resolution XPS spectra of (d) Cu 2p and (e) N 1s for SiTCM(Cu). (f) CO_2 adsorption isotherms.

The capacities of CO_2 adsorption on SiT, SiTC, SiTCM and SiTCM(Cu) are compared in Fig. 2f, in which the adsorption isotherm of SiTCM(Cu) displays a CO_2 absorption capacity of 1.31 $cm^3\ g^{-1}$ at 800 mmHg, slightly higher than that of SiTCM (1.22 $cm^3\ g^{-1}$ at 800 mmHg). Similar CO_2 absorption on SiTCM and SiTCM(Cu) indicates the same topological structure of the MOFs with similar specific surface areas and pore characteristics, and that the metalloporphyrin Cu centers impose a limited impact on CO_2 absorption.[31] In contrast, CO_2 absorption is only 0.79 $cm^3\ g^{-1}$ at 800 mmHg for SiTC and 0.65 $cm^3\ g^{-1}$ at 800 mmHg for SiT; both are significantly inferior to the MOF-functionalized photocathodes. Therefore, the MOF scaffolds on SiTCM and SiTCM(Cu), when employed as PEC cathodes for the CO_2RR, are expected to promote the reactive surface area and CO_2 concentration at the electrode/electrolyte interface, which will be closely examined in the following photoelectrochemical studies.

As carboxylic MOFs are typically unstable in aqueous alkaline electrolytes, the PEC CO_2R performances of SiTCM(Cu), SiTCM and other control samples were assessed in a mixed MeCN/H_2O (10 : 1) electrolyte containing 0.1 M tetrabutylammonium tetrafluoroborate ($TBABF_4$) under visible light (100 mW cm^{-2}, AM 1.5G, $\lambda > 420$ nm). Acetonitrile was chosen as the major solvent to enhance the CO_2 solubility, while water plays an important role in providing protons for CO_2 reduction, which typically involves proton-coupled electron transfer. The MOF-modified electrodes were quite stable in this type of mixed electrolyte, as evidenced by the unchanged surface morphology (Fig. S7†) and the ATR-IR spectrum (Fig. S8†) after immersing SiTCM(Cu) in a mixed electrolyte for one week. The ratio of MeCN/H_2O (10 : 1) was verified by PEC experiments to produce the best performance of the CO_2RR (Fig. S9†). Meanwhile, we found that the temperature of the electrolyte did not increase with continuous irradiation after an early surge of about 10 degrees (Fig. S10†). Fig. 3a shows a comparison of the linear sweep voltammograms (LSVs) of SiT, SiTC, SiTCM and SiTCM(Cu). As expected, all these photocathodes displayed a negligible current density in the dark owing to the insulative p-type nature of the Si substrate (Fig. S11†). Upon illumination, the photocurrent rose quickly once the onset potential was surpassed. While the total current density followed the order: SiT < SiTC < SiTCM < SiTCM(Cu), the onset potential obeyed an opposite trend. Of particular note, SiTCM(Cu) produced a large current density of 16.5 mA cm^{-2} at −3.0 V (*vs.* Fc/Fc^+) and a high onset potential of −1.25 V (*vs.* Fc/Fc^+), far outperforming those reported in the literature with similar electrolytes.[15,23,35]

Gas chromatography (GC) was employed to monitor the gaseous products obtained during the potentiostatic PEC processes on all photocathodes. Fig. 3b shows that at applied potentials swept from −1.7 to −2.9 V (*vs.* Fc/Fc^+) all the chronoamperometric *i*–*t* curves of SiTCM(Cu) maintained a stable photocurrent output that is consistent with the LSV curve in Fig. 3a. Only H_2 and CO were detected by GC, with the sum of their faradaic efficiencies (FEs) being close to 100%. There were no other liquid-phase products detected by ^1H NMR spectroscopy (Fig. S12†). The CO selectivity increased initially with a decrease in potential, attaining a maximal FE of 87% at −2.5 V (*vs.* Fc/Fc^+). Afterwards, the CO selectivity dropped again, retaining 77% at −2.9 V *vs.* Fc/Fc^+ (Fig. 3c). In addition, SiTCM (Cu) manifested fairly good PEC stability in producing CO at both −1.9 and −2.5 V (*vs.* Fc/Fc^+), yielding a steady photocurrent output of ~4.0 mA cm^{-2} (FE_{CO} = ~40%) for a testing period of 8 h and ~10.2 mA cm^{-2} (FE_{CO} > 80%) for 1 h,

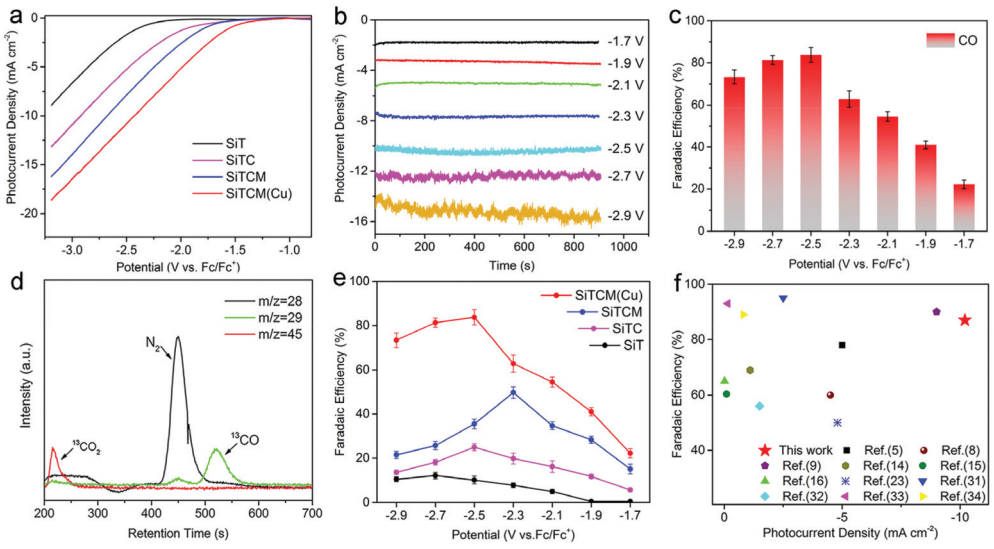

Fig. 3 PEC CO_2R performance of SiTCM(Cu). (a) Comparison of LSVs for SiT, SiTC, SiTCM and SiTCM(Cu) under illumination. (b) Chronoamperometric *i*–*t* curves and (c) CO faradaic efficiencies of SiTCM(Cu) at various potentials. (d) GC-MS spectra of the isotopic $^{13}CO_2$ test on SiTCM(Cu). (e) Comparison of the CO faradaic efficiency of SiT, SiTC, SiTCM and SiTCM(Cu) at various potentials. (f) Comparison of the CO_2RR FE and photocurrent density from this study with recent literature engaging state-of-the-art PEC catalysts (see Table S1† for reference details).

respectively (Fig. S13†). Both IR and SEM characterization studies after the stability tests confirmed that the structure of the MOF scaffolds was well preserved (Fig. S14 and S15†). To assert that the produced CO was exclusively converted from the CO_2 source, rather than organic species such as acetonitrile and $TBABF_4$ presented in the electrolyte, isotopic $^{13}CO_2$ experiments were carried out under identical conditions. After electrolysis at −2.5 V (*vs.* Fc/Fc^+) for 15 min, a syringe sampler was used to feed the produced gas mixture to a tandem gas chromatography-mass spectroscopy (GC-MS). As shown in Fig. 3d, at the retention time of CO the eluent only contained ^{13}CO with an m/z of 29, instead of ^{12}CO with m/z = 28 (Fig. 3e). This observation unequivocally proves that the produced CO solely originated from the CO_2 input.

By comparing the PEC CO_2RR performances on all photocathodes (Fig. 3e), it was found that SiTCM(Cu) exhibited notably higher FEs of CO (FE_{CO}) across the entire potential range from −1.7 to −2.9 V (*vs.* Fc/Fc^+), suggesting that the metalloporphyrin sites contribute extra activity to the CO_2RR. On all photocathodes, the FE_{CO} rose initially with a decrease in potential but then dropped again, implying that at a more negative bias the kinetics of the CO_2RR could be limited by CO_2 mass transport. Note that on SiT, the CO_2RR kinetics was the lowest, and thus the impact from CO_2 mass transport might be the least. The improved CO_2RR performance on SiTCM, when compared to SiTC, was likely due to the enhanced light absorption, as well as the enriched CO_2 concentration at the electrode/electrolyte interface. Furthermore, by comparing SiTCM and SiTCM(Cu) the significantly higher FE_{CO} of the latter after −2.3 V (*vs.* Fc/Fc^+) suggests that the metalloporphyrins enabled suppressing H_2 at a more negative bias, together with a higher CO_2 turnover. Consequently, these comparative studies strongly support that the MOF coating and the metalloporphyrin Cu centers are capable of synergistically promoting the kinetics and selectivity of CO production. To the best of our knowledge, this is the first time MOFs are being integrated with Si-based photocathodes for PEC CO_2RRs. Concerning both the photocurrent density and CO faradaic efficiency, SiTCM(Cu) outperforms the state-of-the-art PEC cathodes reported in the literature involving various photoabsorbers and catalysts (Fig. 3f and Table S1†).[36–38]

To furnish a mechanistic understanding of the superior PEC CO_2R performance of SiTCM(Cu), comprehensive photoelectrochemical analyses were carried out. First of all, electrochemical impedance spectra (EIS) recorded at −2.5 V (*vs.* Fc/Fc^+) under illumination in the CO_2-saturated electrolyte displayed two semicircles for all photocathodes of SiT, SiTC, SiTCM and SiTCM(Cu) (Fig. 4a). The Nyquist plots were fitted to the equivalent circuit shown in the inset of Fig. 4a, where R_s represents the series resistance from solution and ohmic contact, R_1 is the charge transfer resistance from the n^+–p Si substrate to the upper surface coatings, and R_2 originates from the charge transfer resistance at the electrode/electrolyte interface.[39] While the R_s values of all four photocathodes were similar (Table S2†), SiTCM showed a notably smaller R_2 value of 63.8 Ω compared to those of SiTC (100.2 Ω) and SiT (150.5 Ω), corroborating that the introduction of a MOF coating onto the Cu surface promotes the charge transfer kinetics through an enlarged surface area and enriched CO_2 concentration. Among all four photocathodes, SiTCM(Cu) exhibited the smallest R_1 of 11.9 Ω and R_2 of 40.7 Ω, attesting to the further enhanced charge transfer and redox kinetics on account of the prevailing metalloporphyrin sites.

Steady-state photoluminescence (PL) spectra were acquired on SiT, SiTC, SiTCM and SiTCM(Cu) to interrogate the tendency of exciton recombination and the efficiency of charge separation on these photocathodes (Fig. 4b). The severe photoluminescence bleaching on SiTC, when compared to SiT, strongly support that the Cu overlayer helps to suppress radiative recombination of the photoexcited electron–hole pairs through the formation of a Schottky junction. The quenching of photoluminescence was further escalated by the upper MOF coating, as witnessed by the reduced emission intensity on both SiTCM and SiTCM(Cu). Therefore, the multi-junctional architecture of both SiTCM and SiTCM(Cu) helped to promote charge separation, accounting for their superior PEC CO_2RR activity shown in Fig. 3e.

The enhancement in charge separation and transfer efficiency through consecutive Cu and MOF coatings was further verified *via* transient photocurrent response (TPR) measurements by intermittently chopping the light illumination during the CO_2RR (Fig. 4c). At −2.5 V (*vs.* Fc/Fc^+), the photocurrent intensity followed the order SiT < SiTC < SiTCM < SiTCM(Cu), which is in good agreement with their LSV current densities shown in Fig. 3a. Additionally, stable square *i*–*t* waves were recorded on all photocathodes despite an initial current overshoot, further attesting to the outstanding photoelectric sensitivity and stability of the PEC devices.

Taken together from the above analyses and discussions, we are now able to draw a schematic diagram illustrating the PEC process for the CO_2RR on SiTCM(Cu) as shown in Fig. 4d. Upon illumination, the pyramidal Si photoabsorber efficiently harvests light photons and produces electron–hole pairs, which are readily separated by the built-in electric field of the p–n junction at the n^+–p Si surface. At the Si surface, the quenching of photocarriers by surface defects and dangling bonds is effectually suppressed by the TiO_2 overlayer, serving also as a highly potent electron transfer layer. Further through the TiO_2/Cu Schottky junction, the photogenerated electrons can be efficiently relayed to the Cu interlayer and further to the upper catalytic MOF scaffolds for electrochemical CO_2 reduction.

Next, to scrutinize the mechanism of metalloporphyrin Cu centers in catalyzing the CO_2RR, cyclic voltammograms (CVs) were acquired on separately synthesized Cu-TCPP and Cu-TCPP(Cu) electrocatalysts loaded onto glassy carbon electrodes (GCEs) (Fig. 4e). In the Ar-saturated acetonitrile/water (10 : 1) electrolyte, the CV curve of Cu-TCPP(Cu) displays two reversible redox waves at −1.80 and −2.28 V (*vs.* Fc/Fc^+), which can be attributed to the Cu^{II}/Cu^{I} and Cu^{I}/Cu^{0} monoelectronic redox couples, respectively (Fig. 4e, top panel).[40–42] These redox couples, as expected, were not observed on Cu-TCPP due to the lack of metalloporphyrin Cu centers. Note that in

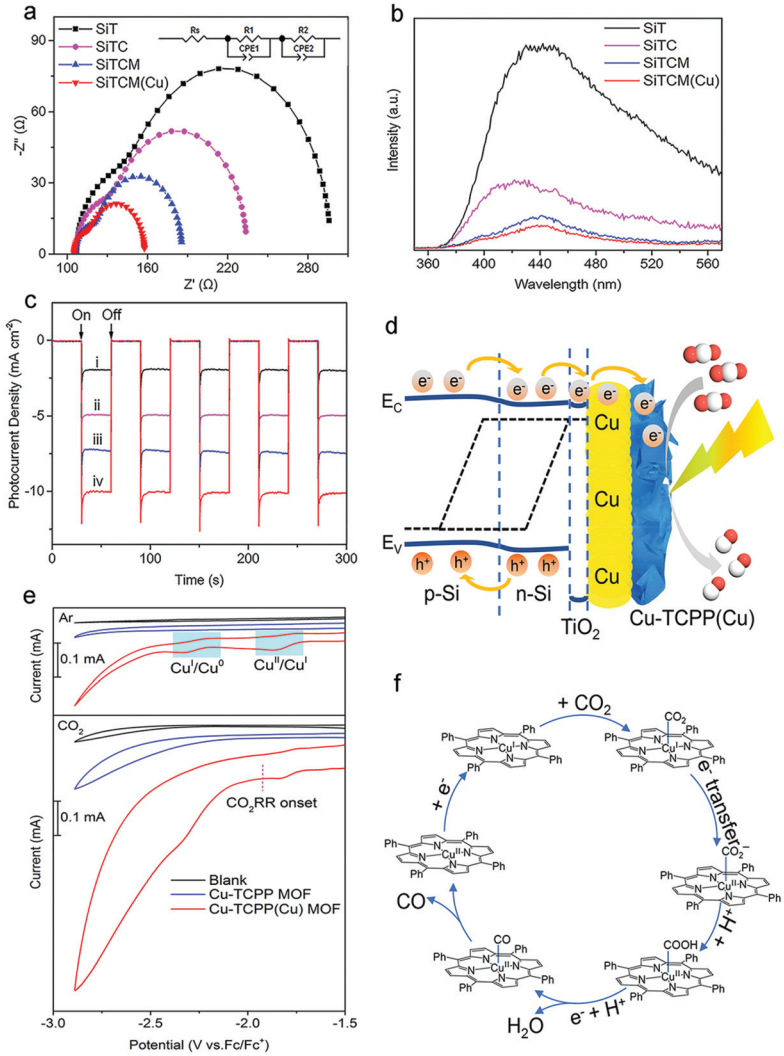

Fig. 4 Photoelectrochemical analyses on the charge kinetics and CO_2RR mechanism. (a) EIS spectra recorded on SiT, SiTC, SiTCM and SiTCM(Cu) under illumination at −2.5 V (*vs.* Fc/Fc$^+$) in the CO_2-saturated electrolyte (inset is the equivalent analogue circuit for spectral fitting). (b) Steady-state PL spectra of SiT, SiTC, SiTCM and SiTCM(Cu). (c) Transient photocurrent responses of SiT (i), SiTC (ii), SiTCM (iii) and SiTCM(Cu) (iv) at −2.5 V (*vs.* Fc/Fc$^+$) in a CO_2-saturated electrolyte. (d) Schematic diagram for the charge transfer scheme of SiTCM(Cu). (e) CVs of Cu-TCPP(Cu), Cu-TCPP and the blank glassy carbon electrode under a Ar/CO_2-saturated electrolyte at a scan rate of 50 mV s^{-1} (electrolyte : MeCN–H_2O (10 : 1) containing 0.1 M $TBABF_4$ solution). (f) Proposed CO_2RR pathway for producing CO on Cu-TCPP(Cu).

Fig. 3a, the LSV onset potential observed for SiTCM(Cu) was at ~−1.25 V (*vs.* Fc/Fc$^+$), which, after being compensated with the photovoltage (in the range of 500–600 mV for the device configuration adopted in this study), coincides with the first Cu^{II}/Cu^{I} reduction wave of Cu-TCPP(Cu) at −1.80 V (*vs.* Fc/Fc$^+$). Such a coincidence suggests that the Cu^{II}/Cu^{I} redox is a prerequisite/correlated with the onset of the CO_2RR on SiTCM(Cu), which occurs earlier than those on SiTC and SiTCM engaging metallic Cu as the catalyst (Fig. 3a). This argument was further testified by CVs acquired in a CO_2-saturated electrolyte, showing the drastically ascending current density on Cu-TCPP (Cu) immediately after the Cu^{II}/Cu^{I} redox wave at −1.80 V (Fig. 4e, bottom panel). Once again, here the significantly enhanced CO_2RR current density on Cu-TCPP(Cu), when compared to Cu-TCPP, reinforces the viewpoint that the metalloporphyrin Cu centers on SiTCM(Cu) play an essential role to boost CO_2 turnovers.

Based on the above interpretations, the CO_2RR pathway on SiTCM(Cu) involving the valence change of metalloporphyrin Cu centers can be proposed in Fig. 4f. The cation of Cu^{2+} at the metalloporphyrin center receives one photoelectron and reduces to Cu^+, which subsequently binds to one of the CO_2 molecules enriched at the Helmholtz layer by the MOF scaffolds. Next, the photoelectron is relayed from Cu^+ to $*CO_2$ and turns the latter into a $*CO_2^-$ anion, and meanwhile the Cu^+ is returned to Cu^{2+}. Subsequently, the $*CO_2^-$ intermediate receives a proton and turns into *COOH, which, after receiving another electron and proton and releasing one H_2O, produces CO as the final product.[43,44] This CO_2RR pathway signifies the role of the valence-variable Cu center and the LMCT process

(ligand to metal charge transfer) of metalloporphyrin in facilitating redox electron transfer, and thus helps to rationalize the greatly improved CO_2RR performance on SiTCM(Cu).

In short, our comparative PEC CO_2RR study on SiTC, SiTCM and SiTCM(Cu) underlines two important facts about the Cu-TCPP(Cu) MOF in synergistically promoting both the kinetics and selectivity of CO production on Si photocathodes. One lies in the extensive MOF scaffold with a 3D porous framework that affords a large reactive surface area and concentrates CO_2 at the electrode/electrolyte interface, while the other relates to the catalytic activity of the metalloporphyrin Cu–N center in promoting electrochemical CO_2 turnover. Additionally, an exquisite photocathode architecture comprising pyramidal n^+–p Si/TiO_2/Cu/MOF multi-junctions with a well aligned band structure further bolsters the light-harvesting and charge-separation efficiency of PEC processes.

Conclusions

In summary, this work, for the first time, integrates MOFs with Si-based photocathodes, attaining a high FE_{CO} of 87% at a photocurrent density of 10.2 mA cm^{-2}, which is amongst the best reported in the literature for the PEC CO_2RR. Through well-devised control experiments and comprehensive photoelectrochemical analyses, the superb performance can be attributed to the exquisite multi-junction design of the photocathode that greatly promotes the photogenerated charge separation and transfer, the 3D porous framework of the MOF scaffold that furnishes a large electrode/electrolyte interface with enriched gas reactants, as well as the highly active metalloporphyrin Cu centers in catalyzing a redox CO_2 turnover. Through the demonstration of the PEC CO_2RR with high current density and product selectivity, this work highlights the application of MOF-based catalysts on elaboratively constructed photocathodes to overcome the charge and mass transport limit of the PEC process.

Conflicts of interest

There are no conflicts to declare.

Acknowledgements

This work was supported by the National Natural Science Foundation of China (No. 22072101, 22075193, 52002259), the National Key R&D Program of China (2020YFB1505703) and the Natural Science Foundation of Jiangsu Province (No. BK20211306). The authors are also grateful for the support from the Honorary Professor Program of Jiangsu Province, the Six Talent Peaks Project in Jiangsu Province (No. TD-XCL-006), and the Priority Academic Program Development (PAPD) of Jiangsu Higher Education Institutions.

References

1 E. Gong, S. Ali, C. B. Hiragond, H. S. Kim, N. S. Powar, D. Kim, H. Kim and S. I. In, *Energy Environ. Sci.*, 2022, **15**, 880–937.
2 J. He and C. Janaky, *ACS Energy Lett.*, 2020, **5**, 1996–2014.
3 S. Xu and E. A. Carter, *Chem. Rev.*, 2019, **119**, 6631–6669.
4 X. Chang, T. Wang, P. Yang, G. Zhang and J. Gong, *Adv. Mater.*, 2019, **31**, 1804710.
5 S. Chu, P. Ou, P. Ghamari, S. Vanka, B. Zhou, I. Shih, J. Song and Z. Mi, *J. Am. Chem. Soc.*, 2018, **140**, 7869–7877.
6 J. T. Song, H. Ryoo, M. Cho, J. Kim, J. G. Kim, S. Y. Chung and J. Oh, *Adv. Energy Mater.*, 2017, **7**, 1601103.
7 G. Gurudayal, J. W. Beeman, J. Bullock, H. Wang, J. Eichhorn, C. Towle, A. Javey, F. M. Toma, N. Mathews and J. W. Ager, *Energy Environ. Sci.*, 2019, **12**, 1068–1077.
8 Q. Kong, D. Kim, C. Liu, Y. Yu, Y. Su, Y. Li and P. Yang, *Nano Lett.*, 2016, **16**, 5675–5680.
9 Y. Hu, F. Chen, P. Ding, H. Yang, J. Chen, C. Zha and Y. Li, *J. Mater. Chem. A*, 2018, **6**, 21906–21912.
10 M. Ding, R. W. Flaig, H. L. Jiang and O. M. Yaghi, *Chem. Soc. Rev.*, 2019, **48**, 2783–2828.
11 X. F. Qiu, H. L. Zhu, J. R. Huang, P. Q. Liao and X. M. Chen, *J. Am. Chem. Soc.*, 2021, **143**, 7242–7246.
12 X. Li and Q. L. Zhu, *EnergyChem*, 2020, **2**, 100033.
13 H. Sun, L. Chen, L. Xiong, K. Feng, Y. Chen, X. Zhang, X. Yuan, B. Yang, Z. Deng, Y. Liu, M. H. Rummeli, J. Zhong, Y. Jiao and Y. Peng, *Nat. Commun.*, 2021, **12**, 6823.
14 B. Shan, S. Vanka, T. T. Li, L. Troian-Gautier, M. K. Brennaman, Z. Mi and T. J. Meyer, *Nat. Energy*, 2019, **4**, 290–299.
15 J. J. Leung, J. Warnan, K. H. Ly, N. Heidary, D. H. Nam, M. F. Kuehnel and E. Reisner, *Nat. Catal.*, 2019, **2**, 354–365.
16 T. T. Li, B. Shan and T. J. Meyer, *ACS Energy Lett.*, 2019, **4**, 629–636.
17 Z. Liang, C. Qu, D. Xia, R. Zou and Q. Xu, *Angew. Chem., Int. Ed.*, 2018, **57**, 9604–9633.
18 Z. Lei, Y. Xue, W. Chen, W. Qiu, Y. Zhang, S. Horike and L. Tang, *Adv. Energy Mater.*, 2018, **8**, 1801587.
19 J. R. Li, R. J. Kuppler and H. C. Zhou, *Chem. Soc. Rev.*, 2009, **38**, 1477–1504.
20 H. Wu, X. Y. Kong, X. Wen, S. P. Chai, E. C. Lovell, J. Tang and Y. H. Ng, *Angew. Chem., Int. Ed.*, 2021, **60**, 8455–8459.
21 L. E. Kreno, K. Leong, O. K. Farha, M. Allendorf, R. P. Van Duyne and J. T. Hupp, *Chem. Rev.*, 2012, **112**, 1105–1125.
22 P. Horcajada, R. Gref, T. Baati, P. K. Allan, G. Maurin, P. Couvreur, G. Ferey, R. E. Morris and C. Serre, *Chem. Rev.*, 2012, **112**, 1232–1268.
23 X. Deng, R. Li, S. Wu, L. Wang, J. Hu, J. Ma, W. Jiang, N. Zhang, X. Zheng, C. Gao, L. Wang, Q. Zhang, J. Zhu and Y. Xiong, *J. Am. Chem. Soc.*, 2019, **141**, 10924–10929.
24 A. Brenneis, J. Overbeck, J. Treu, S. Hertenberger, S. Morkotter, M. Doblinger, J. J. Finley, G. Abstreiter, G. Koblmuller and A. W. Holleitner, *ACS Nano*, 2015, **9**, 9849–9858.
25 Y. Xu and M. A. A. Schoonen, *Am. Mineral.*, 2000, **85**, 543–556.

26 P. E. C. Franken and V. Ponec, *Surf. Sci.*, 1975, **53**, 341–350.
27 C. Li, T. Wang, B. Liu, M. Chen, A. Li, G. Zhang, M. Du, H. Wang, S. F. Liu and J. Gong, *Energy Environ. Sci.*, 2019, **12**, 923–928.
28 H. Li, T. Wang, S. Liu, Z. Luo, L. Li, H. Wang, Z. J. Zhao and J. Gong, *Angew. Chem., Int. Ed.*, 2021, **60**, 4034–4037.
29 S. Neatu, J. A. Macia-Agullo, P. Concepcion and H. Garcia, *J. Am. Chem. Soc.*, 2014, **136**, 15969–15976.
30 Z. Wei, Q. Mu, X. Li, X. Yuan, Y. Su, Z. Deng, Y. Peng and M. Shen, *Adv. Energy Sustain. Res.*, 2021, **3**, 2100134.
31 Y. Zhao, J. Wang and R. Pei, *J. Am. Chem. Soc.*, 2020, **142**, 10331–10336.
32 F. Yu, L. Chen, X. Li, X. Shen, H. Zhao, C. Duan and Q. Chen, *ACS Appl. Mater. Interfaces*, 2021, **13**, 18619–18626.
33 J. Cai, Y. Li, M. Zhang and Z. Li, *Inorg. Chem.*, 2019, **58**, 7997–8002.
34 X. Guo, X. Li, L. Qin, S. Z. Kang and G. Li, *Appl. Catal., B*, 2019, **243**, 1–9.
35 M. Schreier, J. Luo, P. Gao, T. Moehl, M. T. Mayer and M. Gratzel, *J. Am. Chem. Soc.*, 2016, **138**, 1938–1946.
36 S. Roy, M. Miller, J. Warnan, J. J. Leung, C. D. Sahm and E. Reisner, *ACS Catal.*, 2021, **11**, 1868–1876.
37 K. Sekizawa, S. Sato, T. Arai and T. Morikawa, *ACS Catal.*, 2018, **8**, 1405–1416.
38 P. B. Pati, R. Wang, E. Boutin, S. Diring, S. Jobic, N. Barreau, F. Odobel and M. Robert, *Nat. Commun.*, 2020, **11**, 3499.
39 J. Zhao, L. Cai, H. Li, X. Shi and X. Zheng, *ACS Energy Lett.*, 2017, **2**, 1939–1946.
40 N. G. Yasri, T. A. Al-Attas, J. Hu and M. G. Kibria, *Catal. Sci. Technol.*, 2021, **11**, 1580–1589.
41 L. Chen, Z. Guo, X. G. Wei, C. Gallenkamp, J. Bonin, E. Anxolabehere-Mallart, K. C. Lau, T. C. Lau and M. Robert, *J. Am. Chem. Soc.*, 2015, **137**, 10918–10921.
42 Z. Weng, J. Jiang, Y. Wu, Z. Wu, X. Guo, K. L. Materna, W. Liu, V. S. Batista, G. W. Brudvig and H. Wang, *J. Am. Chem. Soc.*, 2016, **138**, 8076–8079.
43 X. K. Wang, J. Liu, L. Zhang, L. Z. Dong, S. L. Li, Y. H. Kan, D. S. Li and Y. Q. Lan, *ACS Catal.*, 2019, **9**, 1726–1732.
44 Y. R. Wang, Q. Huang, C. T. He, Y. Chen, J. Liu, F. C. Shen and Y. Q. Lan, *Nat. Commun.*, 2018, **9**, 4466.